Hyperbranched Quasi-1D Nanostructures for Solid-State Dye-Sensitized Solar Cells

Luca Passoni,[†,‖,#] Farbod Ghods,[†,#] Pablo Docampo,[§] Agnese Abrusci,[§] Javier Martí-Rujas,[†] Matteo Ghidelli,[†] Giorgio Divitini,[⊥] Caterina Ducati,[⊥] Maddalena Binda,[†] Simone Guarnera,[†] Andrea Li Bassi,[†,‡] Carlo Spartaco Casari,[†,‡] Henry J. Snaith,[§] Annamaria Petrozza,[†] and Fabio Di Fonzo[†,*]

[†]Center for Nano Science and Technology@PoliMi, Istituto Italiano di Tecnologia, Via Giovanni Pascoli, 70/3, 20133 Milano, Italy, [‡]Dipartimento di Energia and NEMAS, Center for NanoEngineered Materials and Surfaces, Politecnico di Milano, Via Ponzio 34/3, 20133 Milano, Italy, [§]Clarendon Laboratory, University of Oxford, Parks Road, Oxford, OX1 3PU, United Kingdom, [⊥]Department of Materials Science & Metallurgy, University of Cambridge, Charles Babbage Road, CB3 0FS Cambridge, United Kingdom, and [‖]Dipartimento di Fisica, Politecnico di Milano, Piazza Leonardo Da Vinci 32, 20133 Milano, Italy. [#]L Passoni and F. Ghods equally contributed to this work.

ABSTRACT In this work we demonstrate hyperbranched nanostructures, grown by pulsed laser deposition, composed of one-dimensional anatase single crystals assembled in arrays of high aspect ratio hierarchical mesostructures. The proposed growth mechanism relies on a two-step process: self-assembly from the gas phase of amorphous TiO_2 clusters in a forest of tree-shaped hierarchical mesostructures with high aspect ratio; oriented crystallization of the branches upon thermal treatment. Structural and morphological characteristics can be optimized to achieve both high specific surface area for optimal dye uptake and broadband light scattering thanks to the microscopic feature size. Solid-state dye sensitized solar cells fabricated with arrays of hyperbranched TiO_2 nanostructures on FTO-glass sensitized with D102 dye showed a significant 66% increase in efficiency with respect to a reference mesoporous photoanode and reached a maximum efficiency of 3.96% (among the highest reported for this system). This result was achieved mainly thanks to an increase in photogenerated current directly resulting from improved light harvesting efficiency of the hierarchical photoanode. The proposed photoanode overcomes typical limitations of 1D TiO_2 nanostructures applied to ss-DSC and emerges as a promising foundation for next-generation high-efficiency solid-state devices composed of dyes, polymers, or quantum dots as sensitizers.
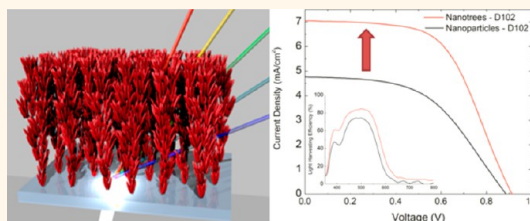
KEYWORDS: dye-sensitized solar cells · hierarchical nanostructures · self-assembled · pulsed-laser deposition · hyperbranched

Solar energy is one of the most promising resources to face the increasing renewable energy demand of the world. Since their introduction in 1991 by Grätzel and co-workers,[1] dye-sensitized solar cells (DSCs) have been widely studied as economical and easy to fabricate solar energy conversion devices.[2]

These devices base their operation on the photogeneration of excitons in a sensitizing dye chemisorbed on a mesoporous structure of a large-band-gap semiconductor, most commonly titanium dioxide. After exciton separation, the electron is transferred into the conduction band of the semiconductor, diffuses through this material until it is collected at the anode (typically fluorine-doped tin oxide, FTO), and is transported to the counter electrode through an external circuit. A redox electrolyte is usually employed to regenerate the dye, which is then subsequently regenerated at the counter electrode.[3] More recently, solid-state dye-sensitized solar cells (hereafter ss-DSCs) employing a solid hole-transporting material (HTM) emerged as a promising alternative to standard liquid electrolyte based devices.[4−6] Despite their undisputed potential due to their versatility, their industrialization is still hampered by their typically low efficiency caused by low optical density and, in turn, low photocurrents. In fact, the thickness of ss-DSC photoanodes is typically limited to 2 μm. This is the result of a combination of factors, among which the infiltration with solid organic hole transporters and shorter charge diffusion lengths than in the iodide/triiodide system play a crucial role. Many studies have been focused on the enhancement of power conversion efficiency by

addressing the different physical phenomena and technical features of these devices. Dyes with higher extinction coefficient and durability as well as novel semiconductor architectures to enhance the electron transport on different photoanodes have been studied.[7,8] Photoanodes with advanced light scattering and trapping architecture can guarantee a higher photon—dye interaction, which can lead to higher generated currents and efficient charge transport. While in liquid-dye-sensitized solar cells a wide range of methods, reviewed in previous publication,[9,10] were adopted to achieve this target, few successful examples have been reported for ss-DSCs. As a reference,[11] a blend of small particles, which increase the surface area, and large-scale particles, which enhance light scattering, is studied and shows a 28% increase in performance. One-dimensional nanostructures such as nanofibers[12,13] and nanotubes[14,15] have been also investigated both to improve electron transport (e.g., by channelled conduction) and to favor the HTM infiltration. In fact, even though it has been recently demonstrated that the pore-filling fraction is not a limiting factor for highly optimized photoanodes,[16] novel architectures less affected by this issue would still be beneficial for the development of high-efficiency dye-sensitized solar cells. A photoanode architecture able to couple enhanced light trapping and scattering, facile HTM infiltration, and enhanced electron transport is still missing. This is the aim of the present study.

Here we demonstrate improved optical density and power conversion efficiency in solid-state DSCs with a photoanode architecture comprising an array of quasi-1D hierarchical nanostructures self-assembled from the gas phase. The morphology recalls a forest formed by trees (main structure) having branches and leaves (nanoparticles).[17] The nanoforest exhibits a hierarchical structure with multiscale elongated features alternated with void channels extended across the whole thickness of the photoanode.[18—21] We reported the application of the first generation of these mesostructures to liquid-type DSCs.[22] Although interesting results were obtained, performances still lagged behind the standard mesoporous photoanode mainly due to severe limitations in roughness factor and dye-loading capacity, which translate to lower generated photocurrents. Similar results were obtained in the following years by other groups[23] also with different materials such as Nb_2O_5[24] and Ta:TiO_2.[25] No reports have been published on the application of this photoanode architecture to ss-DSCs. Building on these previous experiences, we developed a second generation of trees with an increased packing density of the branches, thus reaching roughness factors similar to the long optimized mesoporous photoanodes fabricated from sintered nanoparticles. Moreover, the increased density of each single tree increases their

effective refractive index, enhancing their scattering properties. As a result, nanotrees act as integrated broadband scattering elements having length scales on the same order of magnitude as the wavelength of visible light. At a higher hierarchical level, i.e., the forest, these characteristics result in an improved optical absorption, in turn yielding higher short-circuit current and higher power conversion efficiency with respect to the reference mesoporous photoanode.

RESULTS AND DISCUSSION

Material Fabrication and Characterization. In pulsed laser deposition (PLD), an excimer laser ablates a target of the material that is to be deposited inside a vacuum chamber, which can be filled with a selected gas. The laser locally ablates the target and creates a plasma that expands supersonically due to a density gradient between the solid surface of the target and the environment in which the whole process is performed. The ablated species condense on the sample substrate, where a thin film is formed. By varying the background gas pressure and the laser power, it is possible to induce cluster nucleation in the expanding plume and to finely tune the kinetic energy and the deposition mechanisms of the nanoparticles and therefore the morphology of the deposit. In particular, in certain processing windows,[26] it is possible to induce cluster scattering by the working gas, thus causing self-assembly of the quasi-1D nanostructures, ordered in an array structure perpendicular to the surface of growth, with a typical diameter of hundreds of nanometers and heights linear with the deposition time. With respect to previous work[17,22] the introduction of a rotating substrate holder allowed access to a new growth mode at lower pressures, yielding dense and high surface area photoanodes, while maintaining the hierarchical structure previously reported. The substrate rotation enhances the naturally occurring shadowing effects in PLD depositions at high pressures since the deposition angle of each point of the substrate continuously changes. This growth mechanism resembles that of glancing angle deposition[27] without the need for high tilt angles and sophisticated substrate motion control. The morphological characteristics of hierarchical architectures obtained at different experimental conditions and after 2 h of thermal treatment at 500 °C are shown in the SEM images in Figure 1 together with the reference film obtained by doctor blade coating of an acidic nanoparticle paste in ethanol solution.

In summary, the background gas pressure acts as a coarse tuning parameter, while the substrate rotation extends the processing window, where it is possible to obtain hierarchical structures toward lower pressures.

In fact, similar to previous reports[15,23] with a stationary substrate holder, dense and low surface area films are obtained for TiO_2 deposition at pressures lower than 10 Pa in O_2, due the high kinetic energy
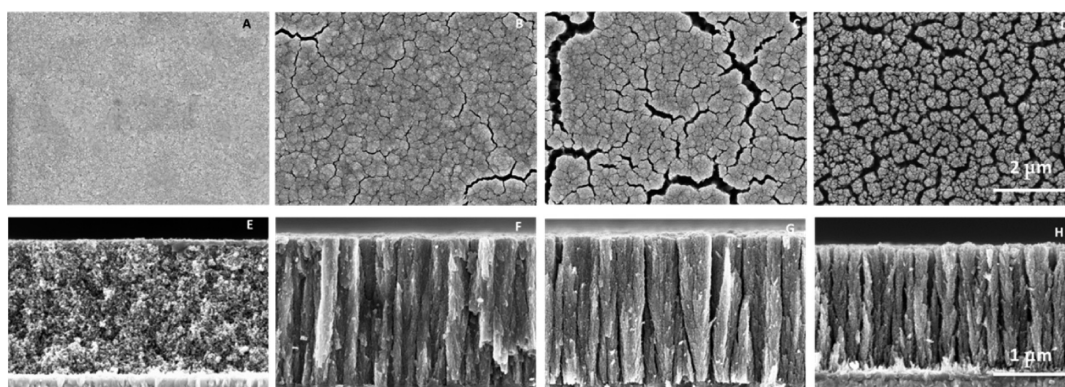
Figure 1. Top view SEM images of (A) nanoparticle paste and PLD films at (B) 5 Pa, (C) 7 Pa, and (D) 10 Pa. Cross section SEM images of (E) nanoparticle paste and PLD films at (F) 5 Pa, (G) 7 Pa, and (H) 10 Pa.
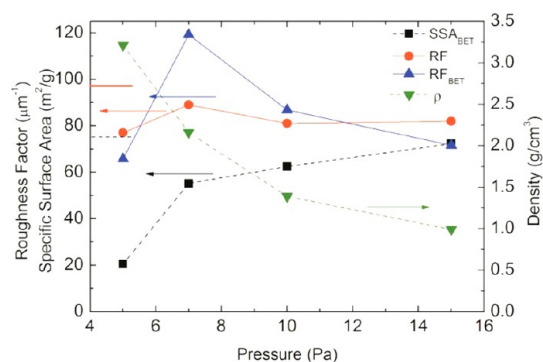

Figure 2. BET specific surface area (SSA_{BET}), density (ρ), and roughness factor (RF and RF_{BET}) for the different samples analyzed. The horizontal lines on the left axis show the values of the standard nanoparticle device.

of the expanding species and reduced scattering from the background gas. This is the case for static deposition at 5 and 7 Pa (Figure (SI) 1). The rotating substrate lowers this threshold, and the nanotrees are obtained down to a pressure of 5 Pa (Figure 1). For very high pressures, large clusters form in the gas phase, diffusing through the background gas to the substrate, thus forming highly disordered materials typical of low-energy deposition processes.[25] Moreover substrate rotation allows larger areas to be deposited, moving from a few square millimeters to a few square centimeters (more technical details can be found in Supporting Information Figure (SI) 2). In general, for a given target material, the threshold pressure depends on various process parameters such as target–substrate distance, laser pulse energy, ambient gas reactivity, and molar mass.[26] In order to characterize the area available for dye anchoring, the roughness factor per unit thickness (RF) (*i.e.*, the ratio between effective and geometric surface area) was measured by a dye (N719) desorption method, showing an optimum deposition pressure of 7 Pa; see Figure 2. Since the roughness factor determines the surface area per unit volume for a given thickness, it can also be estimated by multiplying the surface area per unit weight times the density of the sample. This quantity will be named

RF_{BET} since the specific surface area was characterized by the Brunauer–Emmett–Teller (BET) technique on samples of known weight. RF is expected to be always lower than RF_{BET} since, due to the large difference in probe size, dye, and N_2, respectively, not all the surface accessible to N_2 will be accessible to the dye. As-deposited structures, at all pressures, present an extremely high surface area (up to 350 m^2/g, not shown) that is reduced by an average 5-fold factor after thermal treatment at 500 °C to 20, 55, 62, and 72 m^2/g for samples deposited respectively at 5, 7, 10, and 15 Pa, still comparable with the value of the reference standard photoanode of 75 m^2/g. The density of the structurally more stable deposits was estimated by weighing deposits of known area and thickness. While film density decreases with pressure, the specific BET surface area increases. It is interesting to note that in the case of pressures lower than 7 Pa RF_{BET} is limited by the low surface area, while for higher pressures by the low density. The RF_{BET} has a maximum for photoanodes fabricated at 7 Pa, in accordance with the RF measured by the dye method. Parallel to density, the average pore diameter (see Figure (SI) 3) increases from 5 nm for the 5 Pa sample to 19 nm at 15 Pa, with the optimal sample at 12 nm, while the reference photoanode has an average pore diameter of 20 nm. To compare the two architectures, the full distribution of pore sizes should be considered. In fact, PLD samples exhibit a much wider pore diameter distribution arising from the hierarchical nature of the material itself: nanometer-sized pores within the inner core of the trees, larger pores embedded between each branch, and straight vertical channels up to hundreds of nanometers among the nanotrees. This phenomenon is not present in the nanoparticle paste sample, where the pore size distribution is more uniform and peaked around the average nanoparticle diameter.

Besides higher surface area, trees deposited at 7 Pa and thermally treated at 500 °C for 2 h have a complex hyperbranched structure with an overall conical envelope forming an angle of 15–20 degrees to the tree
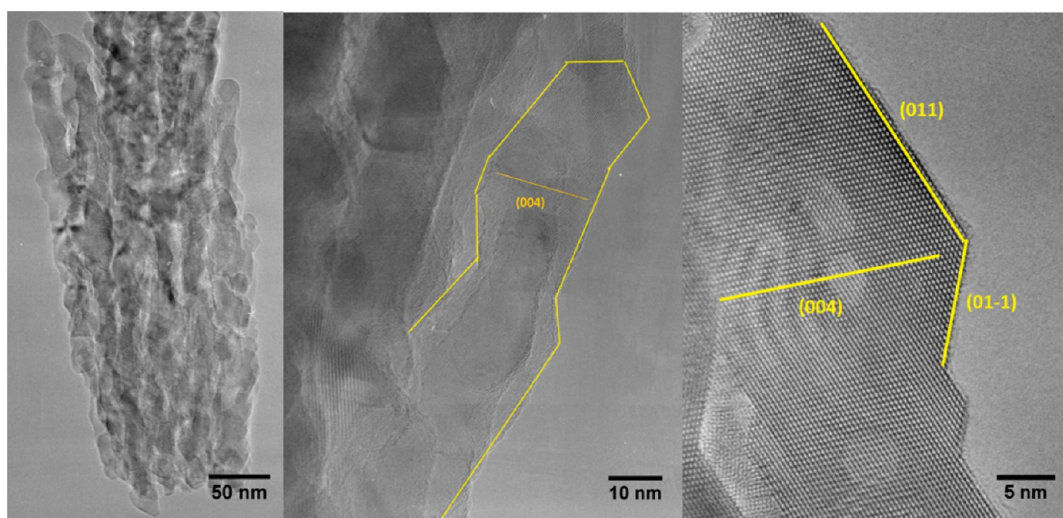
Figure 3. High-resolution TEM images of PLD deposited film at 7 Pa. Here it is possible to appreciate the hyperbranched structures (left-hand side and center), the single crystals with (011)-type surface terminations, and sets of (004) planes running perpendicular to the branch (right-hand side) seen along the [100] zone axis.

growth axis. Figure 3 shows the transmission electron microscope (TEM JEOL 4000EX at 400 kV) images of the TiO_2 film. TEM and high-resolution TEM images show single-crystalline branches developing in the c direction with a characteristic size of 50 to 100 nm. The measured lattice spacings match the anatase TiO_2 structure. Lattice fringes are well resolved even at the outer surface, confirming the high crystallinity of the branches. As shown in Figure 3, the branches display continuity of lattice planes, and surfaces are preferentially terminated with (011)-like planes. As reported in the literature, hyperbranched structures of anatase TiO_2 are preferentially enclosed by a majority of (011)/(101)-type facets on the longitudinal walls and can be terminated by (001)-type facets at the opposite basal sides.[20] This particular growth configuration is thought to be a phenomenon arising in order to minimize the total free energy during crystallization in a mechanism similar to oriented attachment.[10,21] The high film density in the case of the PLD 7 Pa sample allows primary crystal seeds to undergo a free energy minimization process, which does not occur in the case of less dense morphology (higher deposition pressures). The preferential growth along the c axis was confirmed by X-ray diffraction (XRD) spectra of TiO_2 film as shown in Figure 4. Indeed, the peak intensity ratio of (004) to (101) in the XRD spectrum of anatase is equal to 1.33 for PLD film deposited at 7 Pa, which, compared to the powder value of 0.198, is a clear indication of the strong preferential growth along the [004] direction.[21] It is worth noting that the rutile phase appears, even though just in traces, in samples deposited at 10 and 20 Pa.

Optical Characterization. The optical characteristics of the photoanodes after thermal treatment are evaluated with a UV/vis spectrophotometer (see Experimental Section) on bare titanium dioxide deposited at different
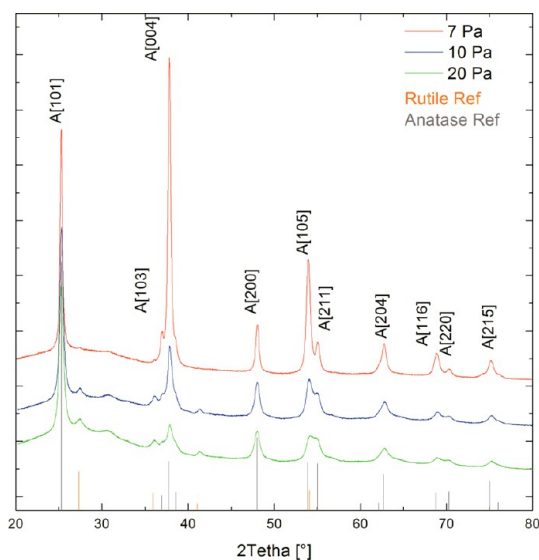

Figure 4. XRD spectra of PLD samples deposited at 7, 10, and 20 Pa compared with the reference XRD spectrum of TiO_2 nanopowder.

pressures to quantify their light-scattering properties. A standard thickness of 1.7 μm, typical of ss-DSC, was chosen. The multiscale nature of the nanotrees, with a pseudocone shape, introduces scattering elements with a high effective refractive index and increasing characteristic size from the glass substrate upward.[28] In this way we obtain a condition where, for an extended range of wavelengths, a large fraction of the light emerges from the photoanode at an angle higher than 4 degrees, as shown in Figure 5a. This high scattering efficiency, coupled with the metallic back reflector (the Ag contact), effectively multiplies the optical path within the photoanode. In Figure SI (5) the haze factor of the photoanodes grown at different pressures, defined as the diffuse over the total transmittance, is

plotted as a function of wavelength. The optimum, achieved at a deposition background pressure of 7 Pa, enabled scattering of 40−80% of the transmitted light over the whole visible range.

The total transmittance and haze factor of all devices fabricated with PLD at different pressures and with standard nanoparticle paste can be found in the Supporting Information in Figure (SI) 5. An important feature highlighted by the graphs in Figure (SI) 5 is that the scattering does not have a predominant backward component. Indeed, total transmittance is reduced by a small factor, while its diffuse component is increased significantly in PLD photoanodes, which therefore
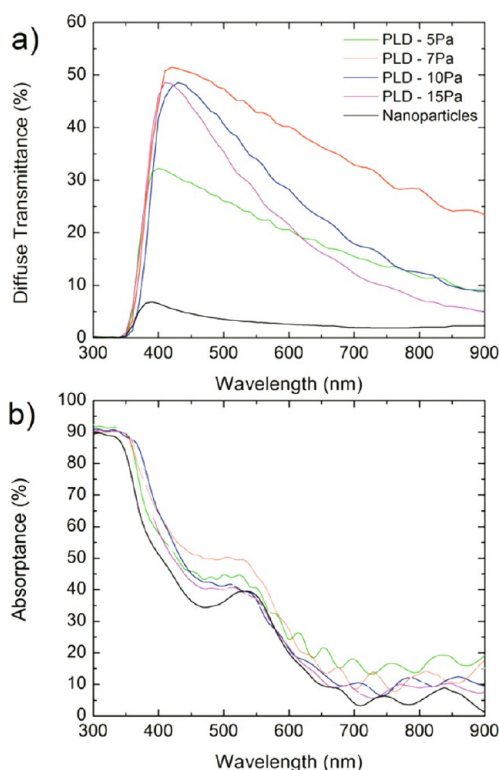

Figure 5. Optical analysis of devices fabricated at different pressures by pulsed laser deposition compared with a standard nanoparticle mesoporous layer. (a) Diffuse transmittance and (b) absorptance.

scatter the light within the device, increasing its optical density. In turn, after sensitization with the N719 dye, the probability of photon−dye molecule interaction and therefore absorptance is increased as shown in Figure 5b[29] by up to 37.5% compared to the nanoparticles reference. Given that the roughness factor is generally lower than the reference (between −21% and −8%), we attribute the enhancement in optical density to the particular light-scattering characteristics of the hierarchical photoactive layer. Subtracting the absorptance of glass, FTO, the compact layer, and bare TiO_2 from those of the same system with TiO_2/dye, the light harvesting efficiency (LHE actually connected to photogeneration) was obtained (Figure 6a). By integrating the LHE spectra in the visible range (350−750) multiplied by the solar photon flux AM1.5 and assuming 100% internal quantum efficiency (IQE) (*i.e.*, each absorbed photon is converted into charge carrier transported to the electrode), it is possible to estimate the maximum expected photogenerated current density values for different devices. The maximum photocurrents attainable from the hierarchical and nanoparticle photoanodes were estimated to be 6 and 4.6 mA/cm^2, respectively, showing a 30% increase. A more detailed optical analysis of the transmittance, conducted at different stages of the device fabrication to isolate the contribution of each cell component, can be found in the Supporting Information.

Photovoltaic Performance Characterization. In preliminary test screening on hierarchical photoanodes prepared at different conditions (5, 7, 10, 15, and 20 Pa, not reported), samples prepared at 7 Pa emerged as the best, coherent with the results of the optical characterization. Table 1 shows the photovoltaic performance for the optically optimized photoanode, whereas in Figure 6b the best device performance is presented. Full statistics are presented in the Supporting Information (Figure (SI) 8).

External quantum efficiency (EQE) measurements were performed on typical devices produced using PLD and mesoporous photoanodes. EQE spectra were divided by the LHE spectra to derive the internal
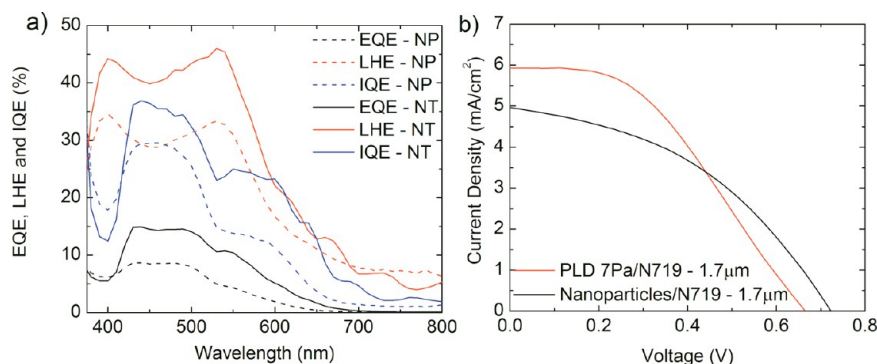

Figure 6. Light harvesting efficiency (red), EQE (black), and IQE (blue) spectra for nanotrees fabricated by PLD at 7 Pa (solid line) and for standard nanoparticle paste (dotted line). (b) Best devices' *J*−*V* curves for device optically optimized nanotrees (red) and reference nanoparticle standard (black) fabricated with N719 dye.

quantum efficiency of both device types (Figure 6a). We consider the higher IQE of the PLD photoanodes to be a result of the particularly elongated structure of the hierarchical material, which creates a preferential pathway for the photogenerated electron collection. The average IQE was estimated by dividing the measured photogenerated current density at short circuit by that estimated by LHE spectra integration.

For the nanotrees, between 350 and 750 nm, we estimate an average IQE of 35% compared to that of nanoparticle-based devices of 27% (+30%). In order to check if this striking increase in performance is maintained in the case of high extinction coefficient dye molecules, we fabricated devices with D102 organic dye (for experimental details refer to ref 30). In Figure 7 we report the LHE of the devices fabricated using D102 dye. When integrated, these spectra yield maximum expected photocurrents of 9.22 and 6.87 mA/cm^2 for nanotree-based and for nanoparticle-based standard devices, respectively (+34%). This is confirmed by the actual value of the short-circuit current obtained in the best performing devices, 7.02 and 4.76 mA/cm^2 for optimized nanotrees and standard nanoparticles, respectively (+47%). Due to similar V_{oc} (0.91 V vs 0.89 V)

and slightly better fill factor values (57.0% vs 50.5%), a substantially higher (+66%) power conversion efficiency was obtained (3.96% vs 2.29%) in the case of devices fabricated with the nanotree-based photoanode architecture. It is worth noting that the efficiency of the PLD devices is among the highest reported for devices fabricated similarly with D102 dye and Spiro-OMeTAD.[31,32] Moreover, it is even higher than the values obtained with volatile electrolyte DSCs in previous works on similar photoanodes.[22,23,25] In order to probe the transport and recombination characteristics of the devices, measurements of photovoltage and photocurrent transients were performed on devices fabricated with D102 dye on a 1.7 μm thick photoanode. In Figure 8 we show the charge lifetime as a function of charge density for standard nanoparticle-based photoanodes and for the PLD fabricated one. The measurements are performed in open-circuit and short-circuit conditions. At open circuit the photogenerated charge decay represents the recombination characteristics of the devices; a longer lifetime corresponds to lower charge recombination within the device. While the PLD nanotrees appear to exhibit slightly slower recombination at the same charge density, the differences are minor and well within sample to sample variations. This is consistent with photoanodes exhibiting similar surface areas. At short-circuit conditions, the photogenerated charge decay provides information about the time required for charges to exit the device. Again, the PLD-grown and the standard nanoparticle photoanodes behave very similarly, with overlapping points at high light intensities. This is likely due to the fact that while the larger crystalline domain size of PLD photoanodes should in principle boost electron transport, the high packing density between the PLD branches (which yields the high surface area) is such that a high number of interfaces is present between them.[33]

Besides the similar behavior at equal charge density (chosen because of its more relevant physical
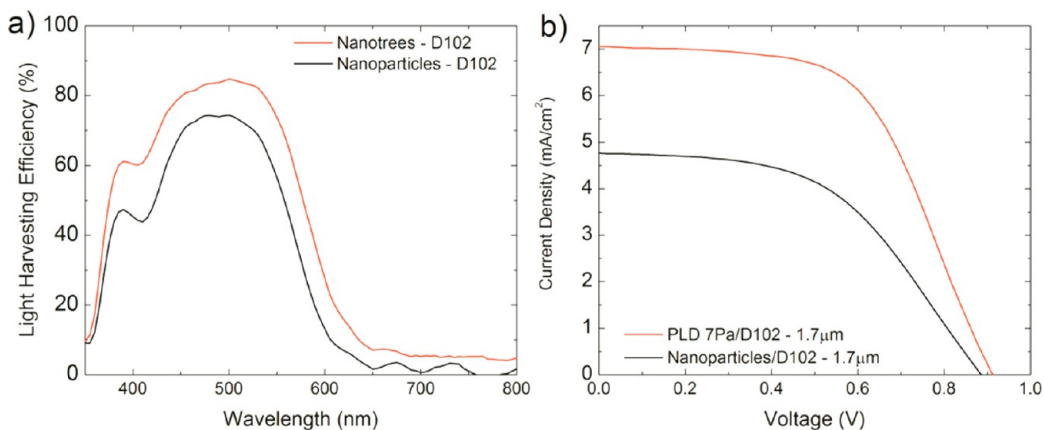
TABLE 1. Best and Average Photovoltaic Performance of the PLD-Based Devices Sensitized with N719 Dye and Fabricated with the Optically Optimized Photoanode Anode and of the Nanoparticle Standard Device

N719	open-circuit voltage (V)	short-circuit current (mA/cm^2)	fill factor (%)	η (%)
nanotrees (7 Pa) best	0.67	5.92	41.14	1.77
nanoparticles best	0.72	4.88	41.90	1.56
increment (%)	−6.94	+21.31	+1.81	+13.46
nanotrees (7 Pa) average	0.70	2.70	45.55	0.86
nanoparticles average	0.72	2.00	44.38	0.64
increment (%)	−2.72	+35.06	+2.65	+34.37

Figure 7. Light harvesting efficiency (LHE) (a) and $J−V$ characteristic (b) of the device sensitized with D102 dye.
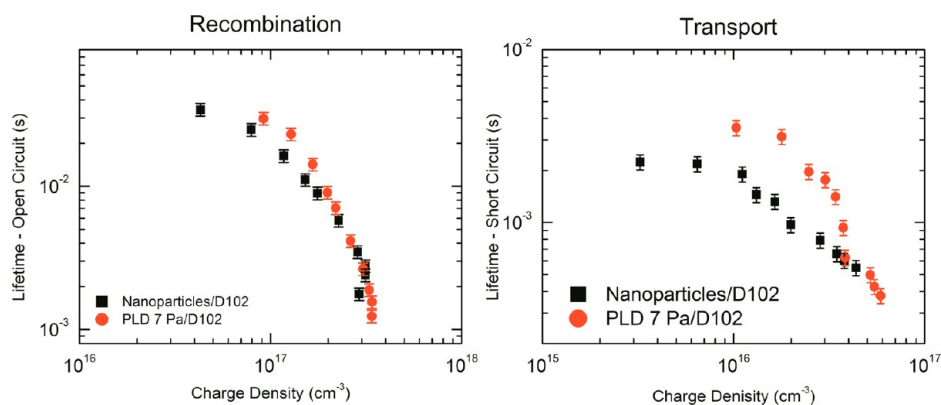
Figure 8. Photovoltage and photocurrent measurements of devices fabricated with a standard nanoparticle photoanode and a PLD fabricated one. The devices are 1.7 μm thick with Spiro-OMeTAD as HTM material and D102 dye.
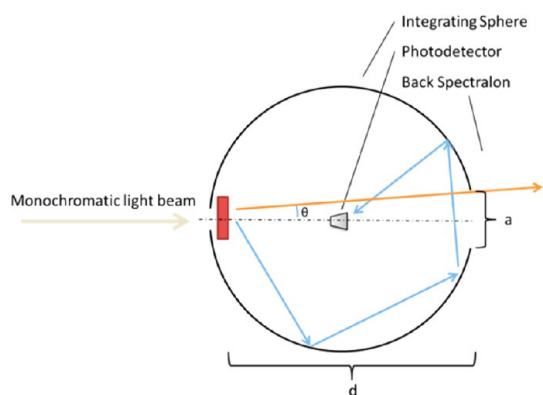

Figure 9. Schematic of the spectrophotometer setup used for measuring diffused transmittance. The same setup is also used to measure the total transmittance by applying a 100% reflective mirror to impede the nonscattered light from exiting the sphere.

meaning) at this point it is worth noting that, as a result of higher optical density of the hyperbranced nanotrees, the charge density at equal illumination intensity is increased for PLD photoanodes. This is thought to lead to better saturation of trap states and consequently to slightly faster electron transport. Enhanced

optical properties therefore lead to higher charge photogeneration and thus better photovoltaic performances.

CONCLUSIONS

We have demonstrated a self-assembled growth from the gas phase of an array of hierarchical TiO$_2$ mesostructures comprised of anisotropic single-crystalline branches upon thermal annealing. The resulting hyperbranched structure can be grown directly on an FTO-glass substrate without the need for any paste preparation and subsequent processing. Solid-state dye-sensitized solar cell photoanodes were successfully fabricated and characterized, showing significant improvement in power conversion efficiency. This result was mainly due to an increase in photogenerated current resulting from the peculiar hyperbranched structure combining a high roughness factor, broadband light scattering, and efficient electron transport. We believe that this optimized photoanode architecture can be the basic element, a scaffold, to build on state-of-the-art solid-state DSCs and even their liquid electrolyte counterparts.

EXPERIMENTAL SECTION

XRD Measurement. X-ray powder diffraction experiments were carried out on a Bruker D8 Advance diffractometer operating in reflection mode with Ge-monochromated Cu Kα1 radiation (λ = 1.5406 Å) and a linear position-sensitive detector, with a 2θ range of 20−80° and a step size of 0.016°.

TiO$_2$ Photoanode Fabrication. Pulsed laser deposition consists in a pulsed excimer laser (Coherent KrF, λ = 248 nm) focused through a lens and a window, on a target of selected material— in this case TiO$_2$—inside a vacuum chamber.

The laser is used with a pulse repetition rate of 20 Hz with 400 mJ energy per pulse. The target is ablated ejecting a plasma plume toward the substrate where deposition takes place. The substrates are rotated at 10 rpm (0.95 m/s tangential velocity) to regulate both the growth regime and the film uniformity. The kinetics of the recondensations, and thus the morphology of the deposit, is controlled by the target substrate distances (5 cm) and the gas pressure, which directly affects the energy

dispersion of the nanoclusters. In this experiment O$_2$ is used as background gas also to control the stoichiometry of the titanium dioxide deposit. Different gas pressures (see text) are tested, while all the other parameters are kept constant. The thickness of the samples is regulated by setting a specific number of laser pulses.

Device Fabrication. Devices are fabricated growing 1.7 μm thick hierarchical nanostructures on FTO glass (Dyesol, 15 Ω/sq) previously coated with 100 nm of a compact TiO$_2$ buffer layer deposited by spray pyrolysis.

After the depositions of 1.7 μm thick PLD photoanodes, they are thermal treated at 500 °C for 2 h to turn them into anatase phase. The substrates are dipped at 70 °C for 1 h in a 0.5 mM water solution of titanium tetrachloride to passivate the surface defects. Samples are then washed and fired again at 550 °C for other 45 min to burn out the solution residuals. At 70 °C the dye sensitization takes place. For N719 the samples are left dipped in dye for 18 h, while for D102 2 h sensitizations are enough to

ensure complete dye chemisorption (for further details see ref 30).

Spiro-OMeTAD, earlier dissolved in chlorobenzene and added with Li salts and *tert*-butylpyridine, is spin-coated on the sensitized device, and eventually 200 nm thick silver counter electrodes are thermally evaporated.

Optical Characterization. All optical measurements were performed in a UV/vis spectrophometer with an integrating sphere (Perkin-Elmer Lambda 1050 spectrophotometer—Xe lamp) to account for the diffusely transmitted light. The transmittance measurements are carried out placing the sample with the scattering PLD photoanode slightly within the integrated sphere so as to collect completely also the diffuse transmittance but, at the same time, avoiding contributions from the reflectance. The minimum angle ($\theta = 4°$) for considering the transmitted light as diffuse was calculated by considering the aperture diameter ($a = 2.1$ cm) allowing the direct light to exit the integrated sphere and the distance ($d = 15$ cm) of the sample from this aperture.

Solar Simulator and EQE Measurements. Photovoltaic performances were measured with a Newport Sun Simulator (Oriel Sol3A Class AAA solar simulator), employing an opaque mask to define the active area of the solar cells, and the external quantum efficiency was measured with a Newport setup operating in dc mode without bias and in a dark environment.

Conflict of Interest: The authors declare no competing financial interest.

Supporting Information Available: Additional SEM images, pore size distribution, additional optical analysis, and the statistic of current density and efficiency obtained for PLD and reference device. This material is available free of charge *via* the Internet at http://pubs.acs.org.

REFERENCES AND NOTES

1. O'Regan, B.; Gratzel, M. A. Low-Cost, High-Efficiency Solar Cell Based on Dye-Sensitized Colloidal TiO$_2$ Films. *Nature* **1991**, *353*, 737–740.
2. Butler, D. Thin Films: Ready for Their Close-Up? *Nature* **2008**, *454*, 558–559.
3. Hagfeldt, A.; Graetzel, M. Light-Induced Redox Reactions in Nanocrystalline Systems. *Chem. Rev.* **1995**, *95*, 49–68.
4. Bach, U.; Lupo, D.; Comte, P.; Moser, J. E.; Weissörtel, F.; Salbeck, J.; Spreitzer, H.; Grätzel, M. Solid-State Dye-Sensitized Mesoporous TiO$_2$ Solar Cells with High Photon-To-Electron Conversion Efficiencies. *Nature* **1998**, *395*, 583–585.
5. In, C.; Byunghong, L.; Jiaqing, H.; Robert, P. H. C.; Mercouri, G. K. All-Solid-State Dye-Sensitized Solar Cells with High Efficiency. *Nature* **2012**, *485*, 486–489.
6. Bouclé, J.; Ackermann, J. Solid-State Dye-Sensitized and Bulk Heterojunction Solar Cells Using TiO$_2$ and ZnO Nanostructures: Recent Progress and New Concepts at the Borderline. *Polym. Int.* **2012**, *61*, 355–373.
7. Cai, N.; Moon, S.-J.; Cevey-Ha, L.; Moehl, T.; Humphry-Baker, R.; Wang, P.; Zakeeruddin, S. M.; Grätzel, M. An Organic D-π-A Dye for Record Efficiency Solid-State Sensitized Heterojunction Solar Cells. *Nano Lett.* **2011**, *11*, 1452–1456.
8. Snaith, H. J.; Karthikeyan, C. S.; Petrozza, A.; Teuscher, J.; Moser, J. E.; Nazeeruddin, M. K.; Thelakkat, M.; Grätzel, M. High Extinction Coefficient "Antenna" Dye in Solid-State Dye-Sensitized Solar Cells: A Photophysical and Electronic Study. *J. Phys. Chem. C* **2008**, *112*, 7562–7566.
9. Park, N.-G. Light Management in Dye-Sensitized Solar Cell. *Korean J. Chem. Eng.* **2010**, *27*, 375–384.
10. Tetreault, N.; Gratzel, M. Novel Nanostructures for Next Generation Dye-Sensitized Solar Cells. *Energy Environ. Sci.* **2012**, *5*, 8506–8516.
11. Kang, S. H.; Kim, J.-Y.; Kim, H. S.; Koh, H.-D.; Lee, J.-S.; Sung, Y.-E. Influence of Light Scattering Particles in the TiO$_2$ Photoelectrode for Solid-State Dye-Sensitized Solar Cell. *J. Photochem. Photobiol. A* **2008**, *200*, 294–300.
12. Kang, S. H.; Choi, S. H.; Kang, M. S.; Kim, J. Y.; Kim, H. S.; Hyeon, T.; Sung, Y. E. Nanorod-Based Dye-Sensitized Solar Cells with Improved Charge Collection Efficiency. *Adv. Mater.* **2008**, *20*, 54–58.
13. Matt, L.; Lori, E. G.; Justin, C. J.; Richard, S.; Peidong, Y. Nanowire Dye-Sensitized Solar Cells. *Nat. Mater.* **2005**, *4*, 455–459.
14. Galstyan, V.; Vomiero, A.; Concina, I.; Braga, A.; Brisotto, M.; Bontempi, E.; Faglia, G.; Sberveglieri, G. Vertically Aligned TiO$_2$ Nanotubes on Plastic Substrates for Flexible Solar Cells. *Small* **2011**, *7*, 2437–2442.
15. Li, K.-L.; Xie, Z.-B.; Adams, S. A. Reliable TiO$_2$ Nanotube Membrane Transfer Method and Its Application in Photovoltaic Devices. *Electrochim. Acta* **2012**, *62*, 116–123.
16. Docampo, P.; Hey, A.; Guldin, S.; Gunning, R.; Steiner, U.; Snaith, H. J. Pore Filling of Spiro-OMeTAD in Solid-State Dye-Sensitized Solar Cells Determined *via* Optical Reflectometry. *Adv. Funct. Mater.* **2012**, *22*, 5010–5019.
17. Di Fonzo, F.; Casari, C. S.; Russo, V.; Brunella, M. F.; Bassi, A. L.; Bottani, C. E. Hierarchically Organized Nanostructured TiO$_2$ for Photocatalysis Applications. *Nanotechnology* **2009**, *20*, 015604.
18. Melas-Kyriazi, J.; Ding, I. K.; Marchioro, A.; Punzi, A.; Hardin, B. E.; Burkhard, G. F.; Tétreault, N.; Grätzel, M.; Moser, J.-E.; McGehee, M. D. The Effect of Hole Transport Material Pore Filling on Photovoltaic Performance in Solid-State Dye-Sensitized Solar Cells. *Adv. Energy Mater.* **2011**, *1*, 407–414.
19. Kroeze, J. E.; Hirata, N.; Schmidt-Mende, L.; Orizu, C.; Ogier, S. D.; Carr, K.; Grätzel, M.; Durrant, J. R. Parameters Influencing Charge Separation in Solid-State Dye-Sensitized Solar Cells Using Novel Hole Conductors. *Adv. Funct. Mater.* **2006**, *16*, 1832–1838.
20. Jun, Y. W.; Casula, M. F.; Sim, J. H.; Kim, S. Y.; Cheon, J.; Alivisatos, A. P. Surfactant-Assisted Elimination of a High Energy Facet as a Means of Controlling the Shapes of TiO$_2$ Nanocrystals. *J. Am. Chem. Soc.* **2003**, *125*, 15981–15985.
21. Buonsanti, R.; Carlino, E.; Giannini, C.; Atamura, D.; De Marco, L.; Giannuzzi, R.; Manca, M.; Gigli, G.; Cozzoli, P. D. Hyperbranched Anatase TiO$_2$ Nanocrystals: Nonaqueous Synthesis, Growth Mechanism, and Exploitation in Dye-Sensitized Solar Cells. *J. Am. Chem. Soc.* **2011**, *133*, 19216–19239.
22. Sauvage, F.; Di Fonzo, F.; Li Bassi, A.; Casari, C. S.; Russo, V.; Divitini, G.; Ducati, C.; Bottani, C. E.; Comte, P.; Graetzel, M. Hierarchical TiO$_2$ Photoanode for Dye-Sensitized Solar Cells. *Nano Lett.* **2010**, *10*, 2562–2567.
23. Noh, J. H.; Park, J. H.; Han, H. S.; Kim, D. H.; Han, B. S.; Lee, S.; Kim, J. Y.; Jung, H. S.; Hong, K. S. Aligned Photoelectrodes with Large Surface Area Prepared by Pulsed Laser Deposition. *J. Phys. Chem. C* **2012**, *116*, 8102–8110.
24. Ghosh, R.; Brennaman, M. K.; Uher, T.; Ok, M.-R.; Samulski, E. T.; McNeil, L. E.; Meyer, T. J.; Lopez, R. Nanoforest Nb$_2$O$_5$ Photoanodes for Dye-Sensitized Solar Cells by Pulsed Laser Deposition. *ACS Appl. Mater. Interfaces* **2011**, *3*, 3929–3935.
25. Ghosh, R.; Hara, Y.; Alibabaei, L.; Hanson, K.; Rangan, S.; Bartynski, R.; Meyer, T. J.; Lopez, R. Increasing Photocurrents in Dye Sensitized Solar Cells with Tantalum-Doped Titanium Oxide Photoanodes Obtained by Laser Ablation. *ACS Appl. Mater. Interfaces* **2012**, *4*, 4566–4570.
26. Di Fonzo, F.; Tonini, D.; Li Bassi, A.; Casari, C.; Beghi, M.; Bottani, C.; Gastaldi, D.; Vena, P.; Contro, R. Growth Regimes in Pulsed Laser Deposition of Aluminum Oxide Films. *Appl. Phys. A: Mater. Sci. Process.* **2008**, *93*, 765–769.
27. Gonzalez-Garcia, L.; Gonzalez-Valls, I.; Lira-Cantu, M.; Barranco, A.; Gonzalez-Elipe, A. R. Aligned TiO$_2$ Nanocolumnar Layers Prepared by PVD-GLAD for Transparent Dye Sensitized Solar Cells. *Energy Environ. Sci.* **2011**, *4*, 3426–3435.
28. Rockstuhl, C.; Lederer, F.; Bittkau, K.; Carius, R. Light Localization at Randomly Textured Surfaces for Solar-Cell Applications. *Appl. Phys. Lett.* **2007**, *91*, 171104.

29. Haase, C.; Stiebig, H. Optical Properties of Thin-Film Silicon Solar Cells with Grating Couplers. *Prog. Photovoltaics* **2006**, *14*, 629–641.

30. Abrusci, A.; Santosh Kumar, R. S.; Al-Hashimi, M.; Heeney, M.; Petrozza, A.; Snaith, H. J. Influence of Ion Induced Local Coulomb Field and Polarity on Charge Generation and Efficiency in Poly(3-hexylthiophene)-Based Solid-State Dye-Sensitized Solar Cells. *Adv. Funct. Mater.* **2011**, *21*, 2571–2579.

31. Jiang, C. Y.; Koh, W. L.; Leung, M. Y.; Chiam, S. Y.; Wu, J. S.; Zhang, J. Low Temperature Processing Solid-State Dye Sensitized Solar Cells. *Appl. Phys. Lett.* **2012**, *100*, 113901.

32. Crossland, E. J. W.; Noel, N.; Sivaram, V.; Leijtens, T.; Alexander-Webber, J. A.; Snaith, H. J. Mesoporous TiO_2 Single Crystals Delivering Enhanced Mobility and Opto-electronic Device Performance. *Nature* **2013**, *495*, 215–219.

33. Docampo, P.; Guldin, S.; Steiner, U.; Snaith, H. J. Charge Transport Limitations in Self-Assembled TiO_2 Photoanodes for Dye-Sensitized Solar Cells. *J. Phys. Chem. Lett.* **2013**, *4*, 698–703.